Laser absorption spectroscopy of rare and doubly-substituted carbon dioxide isotopologues

Ivan Prokhorov, Tobias Kluge, Christof Janssen

Laser absorption spectroscopy of rare and doubly-substituted carbon dioxide isotopologues

Ivan Prokhorov,[*,†,‡] Tobias Kluge,[†] and Christof Janssen[†,‡]

†*Institute of Environemental Physics, Heidelberg University, Im Neuenheimer Feld 229, 69120 Heidelberg, Germany*

‡*LERMA-IPSL, Sorbonne Univ., UPMC Univ. Paris 06, CNRS, Observatoire de Paris, PSL Research University, F-75005 Paris, France*

E-mail: ivan.prokhorov@iup.uni-heidelberg.de

Abstract

Unambiguous detection of the clumped carbon dioxide isotopologue $^{13}C^{16}O^{18}O$ with isotope ratio mass spectrometry is difficult due to isobaric interference on $m/z = 47$. We present an analytical technique based on direct absorption laser spectroscopy for precise, direct and simultaneous detection of all isotopologues involved in the isotope exchange reaction $^{12}C^{16}O_2 + {}^{13}C^{16}O^{18}O \xleftrightarrow{K} {}^{12}C^{16}O^{18}O + {}^{13}C^{16}O_2$ and of $^{12}C^{16}O^{17}O$. The achieved precision of 2×10^{-5} for the $^{13}C^{16}O^{18}O/{}^{13}C^{16}O_2$ and $^{12}C^{16}O^{18}O/{}^{12}C^{16}O_2$ isotopologue ratios allows to determine the equilibrium constant K of the isotope exchange reaction with an external reproducibility of better than 5×10^{-5} (1σ) after 9 reference-sample comparisons, each comparison requires 7 minutes. The isotopic composition of the pure gas can be simultaneously analysed with a precision of 0.05‰ (1σ) for $\delta^{13}C$ and $\delta^{18}O$, and 0.15‰ (1σ) for $\delta^{17}O$. The instrument deploys two interband cascade lasers (ICL) with center wavelengths of 4.3 µm and 4.4 µm. A custom built

optical cell is designed for single pass and multi pass optical paths (pathlength ratio ≈ 1:100), it allows simultaneous detection of rare and abundant isotopologues. The set up is capable to analyse pure CO_2 samples of ∼100 µmol.

Introduction

Precise measurements of multiply-substituted (clumped) and rare singly-substituted isotopologues augment well-established isotopic methods in cosmochemistry, biogeochemistry, paleoclimate research, atmospheric sciences and other fields of environmental research. Particularly interesting is the temperature-dependent behaviour of ^{13}C and ^{18}O isotopes during carbonates precipitation and in gaseous carbon dioxide, as these isotopes show a slightly higher tendency to form a bond at lower temperatures.[1–5] The effect is used as a temperature proxy for paleoclimate reconstruction,[6,7] biogenic carbonate formation,[8,9] quantification of non-equilibrium effects,[10] quantification of biogenic and anthropogenic sources, and sinks of CO_2 in the Earth atmosphere.[11,12] Similar effects are also observed and studied in other molecular systems, e.g. methane[13] or molecular oxygen.[14]

The analytical techniques for these studies generally rely on isotope ratio mass spectrometry (IRMS) of gaseous samples,[7,15] with the drawback that most isotopologue signals such as $m/z = 45$ or 47 suffer from isobaric interferences (see Table 1 in Prokhorov et al.[16]). For example, the analysis of $^{12}C^{16}O^{17}O$ (relative amount fraction 0.75 ‰) at $m/z = 45$ is hampered by the 15 times more abundant $^{13}C^{16}O_2$. The measurement of the isotopologue $^{13}C^{16}O^{18}O$ on $m/z = 47$ with a statistical abundance of 0.044 ‰ also includes a considerable correction (≈3%) of $^{12}C^{18}O^{17}O$. Hence, a sophisticated correction procedure is required to establish an isotopologue thermometer based on mass spectrometric Δ_{47} measurements.[15,17]

In contrast to IRMS, direct laser absorption spectroscopy (DLAS) offers the advantage of a high isotopologue selectivity, which lets us to directly measure the equilibrium constant K (Eq. 1) of the isotopic exchange reaction $^{12}C^{16}O_2 + {}^{13}C^{16}O^{18}O \xleftrightarrow{K} {}^{12}C^{16}O^{18}O + {}^{13}C^{16}O_2$ as an immediate temperature proxy.[16] The equilibrium constant K is proportional to the

product of absorption signals A and a combination of spectroscopic parameters Σ:[16]

$$K(T) = \frac{[^{13}C^{16}O_2]}{[^{12}C^{16}O_2]} \frac{[^{12}C^{16}O^{18}O]}{[^{13}C^{16}O^{18}O]} = \Sigma \times A. \quad (1)$$

Here we present all relevant aspects for the non-destructive, direct and simultaneous measurement of the five most abundant CO_2 isotopologues as well as the gas preparation and sample processing. The method relies on the use of two interband cascade lasers tuned at transitions of the fundamental ν_3 band around 4.3 µm and 4.4 µm. Direct absorption of CO_2 is realised in a low pressure (3 hPa) gas cell with two absorption paths matched to compensate the dynamic range of the isotopologue abundances. In addition, we discuss the calibration and show a comparison of IRMS and DLAS measurements for selected singly and multiply-substituted isotopologues.

Experimental section

Selection of absorption lines

The line selection has been made on the basis of the usual criteria[18], such as significant isolation from interfering lines, temperature sensitivity of the absorption line strength, and the proximity of an equally strong line of the reference isotopologue. The P and R branches of the fundamental asymmetric stretch ν_3 band centred around 2349 cm^{-1} (4.26 µm) are isolated from potentially interfering species, including hydrocarbons, water, nitrous and sulphur oxides. The isotopic substitution changes the spacing of line transitions, providing a unique fingerprint for each isotopologue. The magnitude of the isotopic shift of the fundamental asymmetric stretch band for six most abundant isotopologues is illustrated in Figure 1.

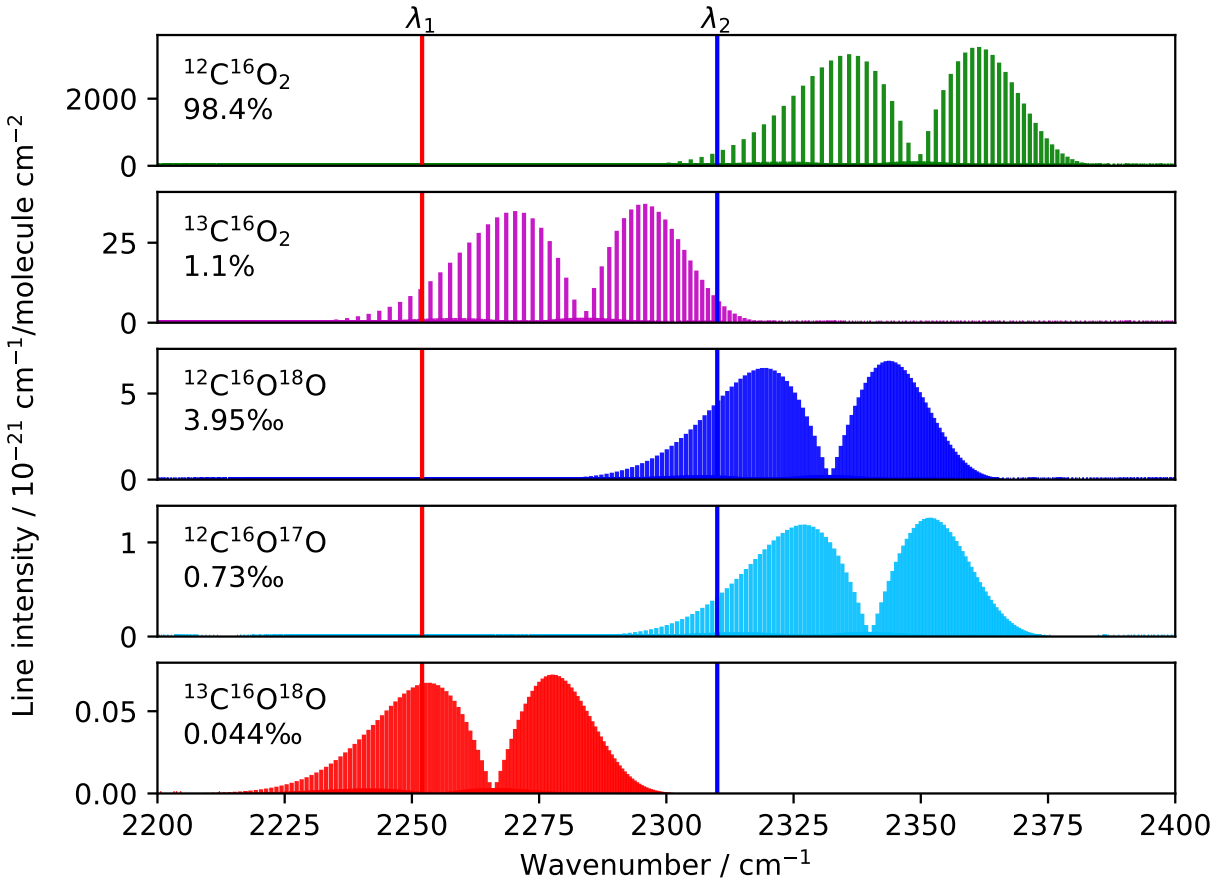

Figure 1: Absorption line positions, intensities and relative abundances of the five major isotopologues of carbon dioxide from HITRAN[19]. Vertical bars indicate the spectral windows assessed by two ICL lasers (λ_1 and λ_2).

Due to the oxygen isotope substitution, the ν_3 P-branch maximum of $^{13}C^{16}O^{18}O$ is centred around 2250 cm^{-1}, where it overlaps with weaker $^{13}C^{16}O_2$ lines in the P-branch of the $02^21 \leftarrow 02^20$ band, providing an almost perfect match in abundance differences. The maximum of $^{13}C^{16}O^{18}O$ is 20 cm^{-1} lower in frequency than the maximum of $^{13}C^{16}O_2$, and significantly less influenced by strong absorption lines of the principal isotopologue. This spectral region has been investigated numerically for the presence of $^{13}C^{16}O^{18}O$ and $^{13}C^{16}O_2$ lines with similar intensities separated by $\leq$0.5 cm^{-1}, and free from interference of other isotopologues. A corresponding search routine has been implemented in Python using isotopologue line positions, intensities and lower state energies from the HITRAN database. The lines listed in the top part of Table 1 have been selected for the isotopologue analysis.

The spectral window around 2310 cm^{-1} (4.33 µm) was introduced by Tuzson et al. [20] and Nelson et al. [21] for the measurements of singly-substituted isotopologues. The corresponding lines are presented in the bottom part of Table 1. We have adopted this spectral region for the measurements of all singly-substituted isotopologues as well as the principal isotopologue using a short light path.

Table 1: Spectroscopic parameters of the absorption lines selected for the clumped isotope analysis. Line positions ν, spectral intensity S, lower state energy E'', and pressure broadening parameter γ are taken from the HITRAN database.

Isotopologue		ν [cm^{-1}]	$S(T_{ref})$ [$\mathrm{cm}^{-1}\,\mathrm{cm}^2$/molec]	E'' [cm^{-1}]	γ [cm^{-1}/atm]
$^{13}C^{16}O^{18}O$	P(17)	2252.6968	6.708×10^{-23}	112.6525	0.101
$^{13}C^{16}O_2$	P(9)	2252.7912	4.750×10^{-23}	1332.5085	0.110
$^{12}C^{17}O^{16}O$	P(35)	2309.9824	4.301×10^{-22}	476.8538	0.086
$^{12}C^{16}O_2$	P(17)	2310.0024	4.868×10^{-21}	1454.9686	0.102
$^{12}C^{18}O^{16}O$	P(27)	2310.2055	4.521×10^{-21}	278.2797	0.093
$^{13}C^{16}O_2$	R(40)	2310.3472	6.720×10^{-21}	639.6307	0.080

The isotopologues line intensity ratio R changes with temperature according to the formula [22] :

$$\frac{\partial R_i^j}{\partial T} \approx \frac{c_2 \left(E_i'' - E_j''\right)}{T^2} \tag{2}$$

where i and j denote transitions of respective isotopologues, E'' is the lower state energy of transition, and c_2=1.438 777 0 cm K the second radiation constant. The selection (Table 1) includes lines from fundamental and combination bands with lower state energies above 1000 cm^{-1}. This imposes a high demand on the thermal stability of the investigated gas sample, because the temperature sensitivity of the line strength can be as high as $2 \times 10^{-8}\,\mathrm{K}^{-1}$, according to Eq. 2. It is especially important for the measurements of the singly substituted isotopologue ratios. The temperature sensitivity of the isotopologue super-ratio K measured according to Eq. 1 depends on the sensitivity difference of two isotopologue ratios:

$$\frac{\partial K}{\partial T} \approx \frac{\partial R_i^j}{\partial T} - \frac{\partial R_k^l}{\partial T} \tag{3}$$

For the selected transitions, the temperature-dependent variation of K is on the level of $7 \times 10^{-10}\,\mathrm{K}^{-1}$.

As shown above, two spectral regions cover selected transitions of five isotopologues. Since the tuning range of the tunable lasers (QCLs, ICLs) is limited to $\sim 1\,\mathrm{cm}^{-1}$, detection can be realised in a scheme with two lasers. However, the characteristic line strength in the 4.33 µm spectral window is approximately 100 times higher than in the 4.43 µm window. To detect all lines simultaneously and to avoid saturation of the strong lines and obtain good signal to noise ration of the weaker lines, we realised an absorption balanced detection scheme[23,24] with two optical paths.

Spectrometer

The spectroscopic instrument deploys two interband cascade lasers (ICL, Nanoplus) with the output power of 1 mW to detect the absorption lines listed in Table 1. Figure 2 shows the layout of the spectrometer. Infrared light is coupled in a 1 m single mode (SM) InF_3 fiber (Thorlabs) by means of a lens collimator (LC). The lasers, the collimating lens, the optical isolators (OI) and their optical mounts are enclosed in a thermally stabilised unit. The unit is a custom made aluminium enclosure, which is thermally coupled to the laser housings. To actively cool the unit with recirculating chillers, channels inside the enclosure were machined.

Optical fibers are used to deliver IR light to the optical cell and to prevent unwanted absorption from CO_2 in ambient air. The light is decoupled into free space by silver reflective collimators (RC). The optical cell has two optical paths: a long folded Herriott type path (multi pass, MP, $L_1 = 10\,\mathrm{m}$) and a short path (single pass, SP, $L_2 = 9.2\,\mathrm{cm}$). The long path is provided by multiple ($N = 58$) reflections between two gold coated concave mirrors with curvature radius $R = 150\,\mathrm{mm}$, which are separated by a distance of 176 mm. The protective gold coating of the mirrors has a reflectance of $R = 97\%$, that leads to an overall transmission factor of about 17%. An off-axis 90° parabolic (OAP) mirror ($EFL = 25.4\,\mathrm{mm}$)

is used to focus the light passing through the cell on the active area of the detector (VIGO PVI-4TE). The short path traverses the cell just once in the direction perpendicular to the optical axis of the Herriott cell. The small volumes between the optical BaF_2 entrance/exit windows and the collimator/detector are purged with dry N_2 (not shown in the figure) to reduce absorption by ambient air CO_2.

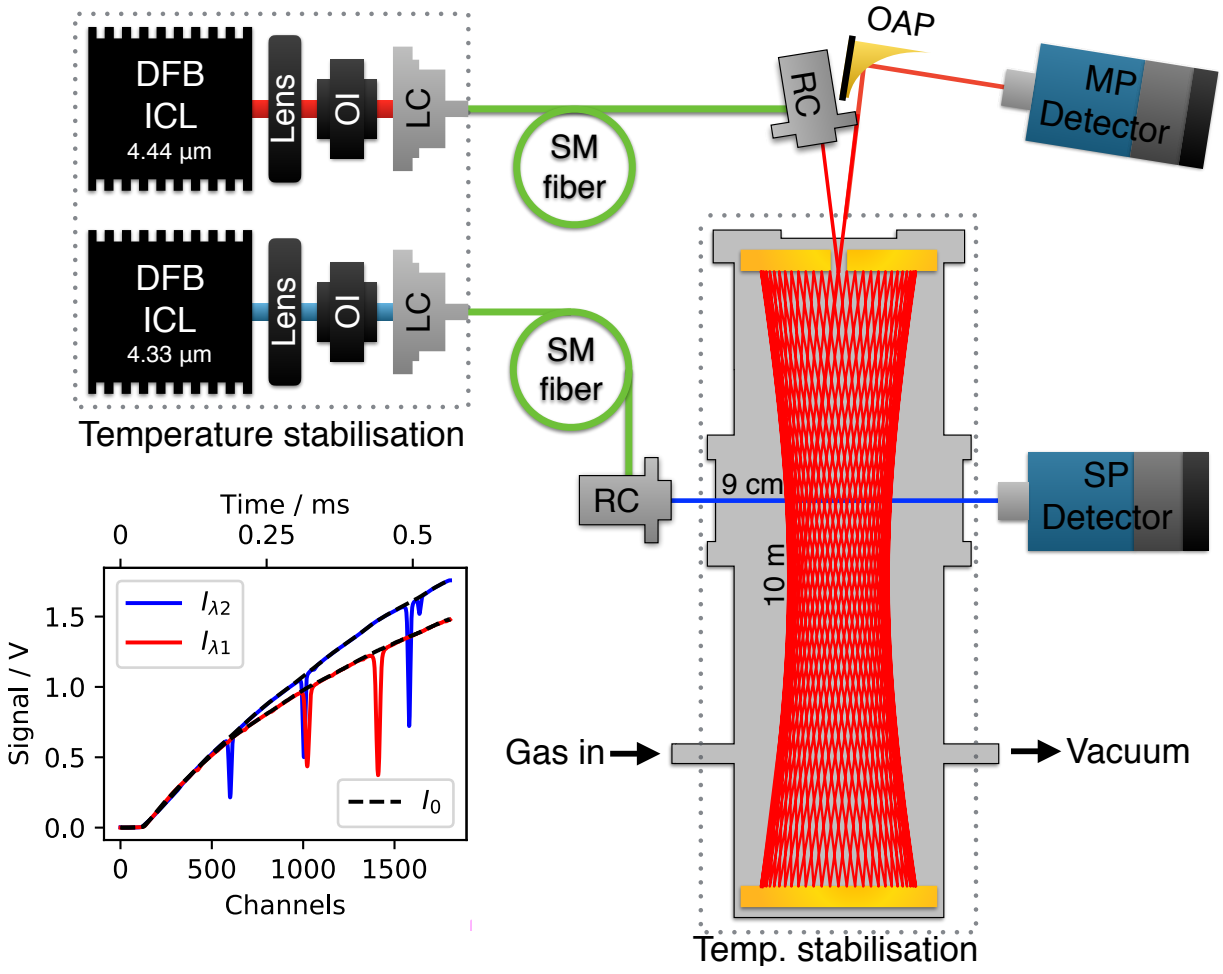

Figure 2: Optical layout of the instrument. Two distributed feedback (DFB) interband cascade lasers (ICL) emit around $\lambda_1 = 4.44\,\mu m$ and $\lambda_2 = 4.33\,\mu m$. The following elements are shown: optical isolator (OI), lens coupler (LC), single mode (SM) fiber, reflective collimator (RC), off-axis parabolic (OAP) mirror, HgCdTe detectors for multi pass (MP) and single pass (SP) optical paths. Multi pass and single pass optical paths are shown in red and blue, respectively. An inset shows an example of acquired raw transmission spectra, $I_{\lambda 1}$ and $I_{\lambda 2}$ – raw signals of λ_1 and λ_2 lasers, I_0 – signals in an empty cell.

The cell is placed inside a cylindrical electropolished stainless steel vacuum chamber,

$V = 800\,\mathrm{ml}$, which is enclosed in a massive thermally stabilised aluminium block. The cell temperature is constantly monitored with a calibrated Pt100 sensor, immersed in the depth of the aluminum block. Two recirculating chillers (ThermoRack 401) are used to thermally stabilise the instrument. One chiller regulates the temperature of the optical train and the optical cell at 297 K, by circulating the coolant through the laser breadboard placed inside the thermally isolated enclosure. The other chiller regulates the temperature of the laser housings at 5 °C. A typical temperature stability of $\pm 2\,\mathrm{mK}(1\sigma)$ has been achieved over the time of a day, despite laboratory temperature variability of $\pm 0.5\,\mathrm{K}$.

The frequency sweep of the lasers is performed by an analog current driver (Toptica DC110) at 1560 Hz, which is modulated by an external voltage ramp. A non-linear waveform $U(t) = U_0 t^\gamma$ current ramp has been applied to linearise the frequency tuning of the lasers. U_0 is a base voltage, t is a time step, and γ is an empirically determined parameter, obtained following a method proposed by Minissale et al.[25] We found optimum values $\gamma_1 = 0.700$ and $\gamma_2 = 0.632$ for the 4.4 µm and 4.3 µm lasers, respectively. The linearity of the frequency tuning has been verified with a Fabry-Perot etalon of free spectral range (FSR) $8.1 \times 10^{-3}\,\mathrm{cm}^{-1}$. Digital discretisation of FSR measurements over 30 channels limits the accuracy of the frequency scale. Uncertainty of the frequency scale is on the level of $\pm 2.7 \times 10^{-4}\,\mathrm{cm}^{-1}$.

Current ramp control and data acquisition is performed by an in-house developed LabView program. The absorption spectrum is acquired at a 3.2 MHz sampling rate over 2048 channels at 16 bit resolution. A custom Python routine has been developed for data post-processing, which includes data averaging, correction for detector dark levels, subtraction of the measured baseline, and spectral fitting. 1560 spectra are averaged over 1 second. Each averaged spectrum is subtracted by a detector dark level, which is measured over the first 80 channels, when the laser modulation current is below the lasing (coherent emission) threshold. A constant offset of 0.6 mV for 4.33 µm and 3.2 mV for 4.44 µm laser has been observed between the detected signals when the respective laser light was blocked and when

the modulation current below the lasing threshold was applied to the laser. A possible explanation of this effect is a side mode emission of the lasers. These values of the offset are subtracted from all measured spectra.

Figure 3 shows the measured transmission spectrum (black dots) and the absorption line fit (colored shaded areas) performed by means of a Levenberg-Marquardt algorithm using the pCqSDHC or Hartmann-Tran[26] profile simplified to a Raution profile according to Table 2 in Ngo et al.[27] The self-pressure broadening parameter γ_L and the velocity changing parameter ν_{VC} have been parametrised as a function of pressure. Parameters have been obtained in a set of separate experiments covering the pressure range from 1.5 hPa to 6.2 hPa. Line positions are taken from HITRAN.[19] The lower panel of Figure 3 depicts the typical level of fit residuals.

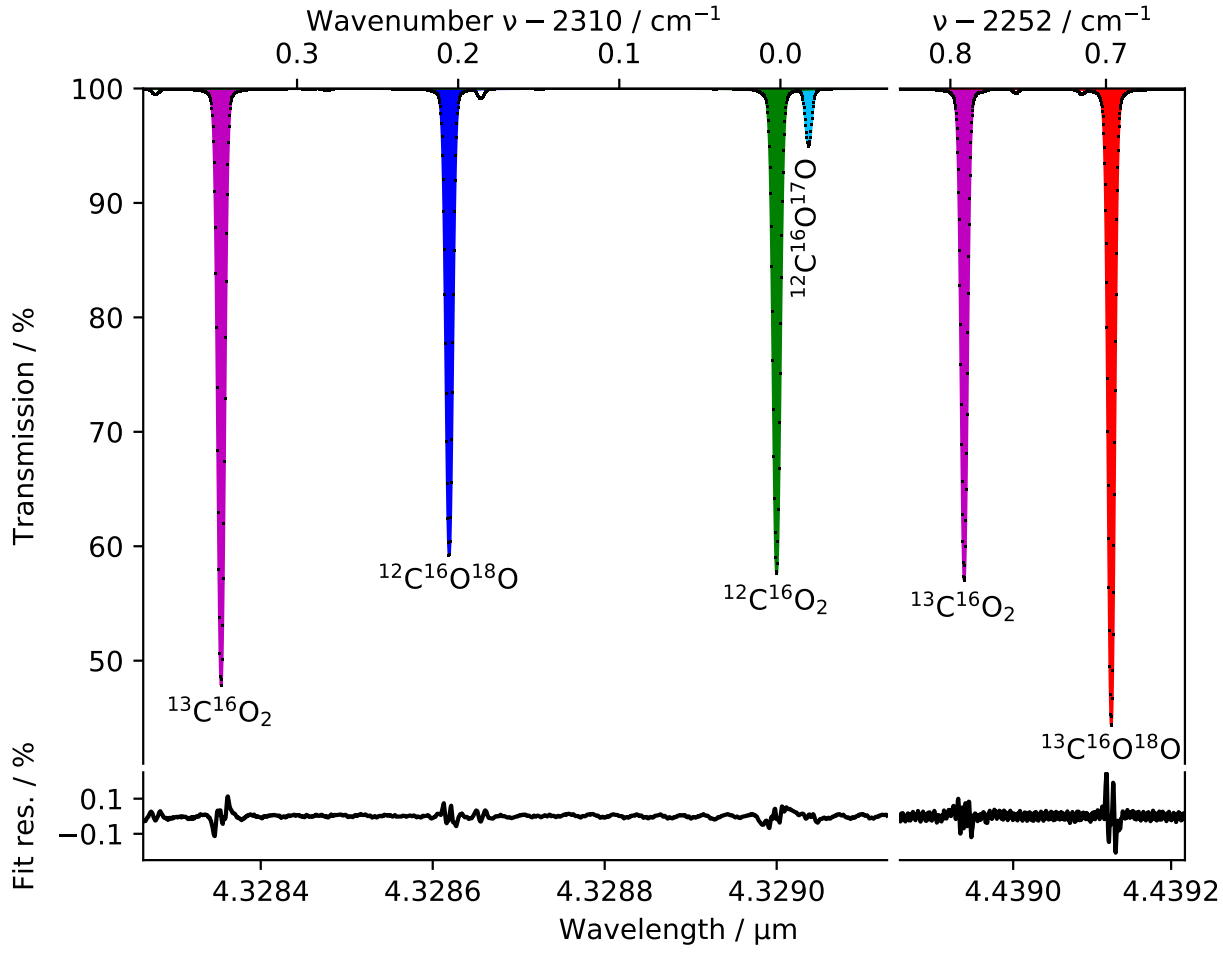

Figure 3: Measured (black dots) and fitted (colored shaded areas) transmission spectrum of pure CO_2 at $T = 297\,\mathrm{K}$ and $p = 3.74\,\mathrm{hPa}$ over the wavelength regions accessible by the tunable lasers used in this study.

Figure 4 shows zoomed part of the transmission spectrum around $2252.7\,\mathrm{cm}^{-1}$ recorded at low pressure ($p = 3.75\,\mathrm{hPa}$). The absorption line is fitted with Rautian profile. The noise level of $\sigma = 1.65 \times 10^{-4}$ at 1 Hz is compareble to state-of-the-art Herriott-type[28] and circular[29] cells. It corresponds to the noise equivalent absorption (NEA) of approximately 5×10^{-5} for $^{13}C^{16}O^{18}O$.

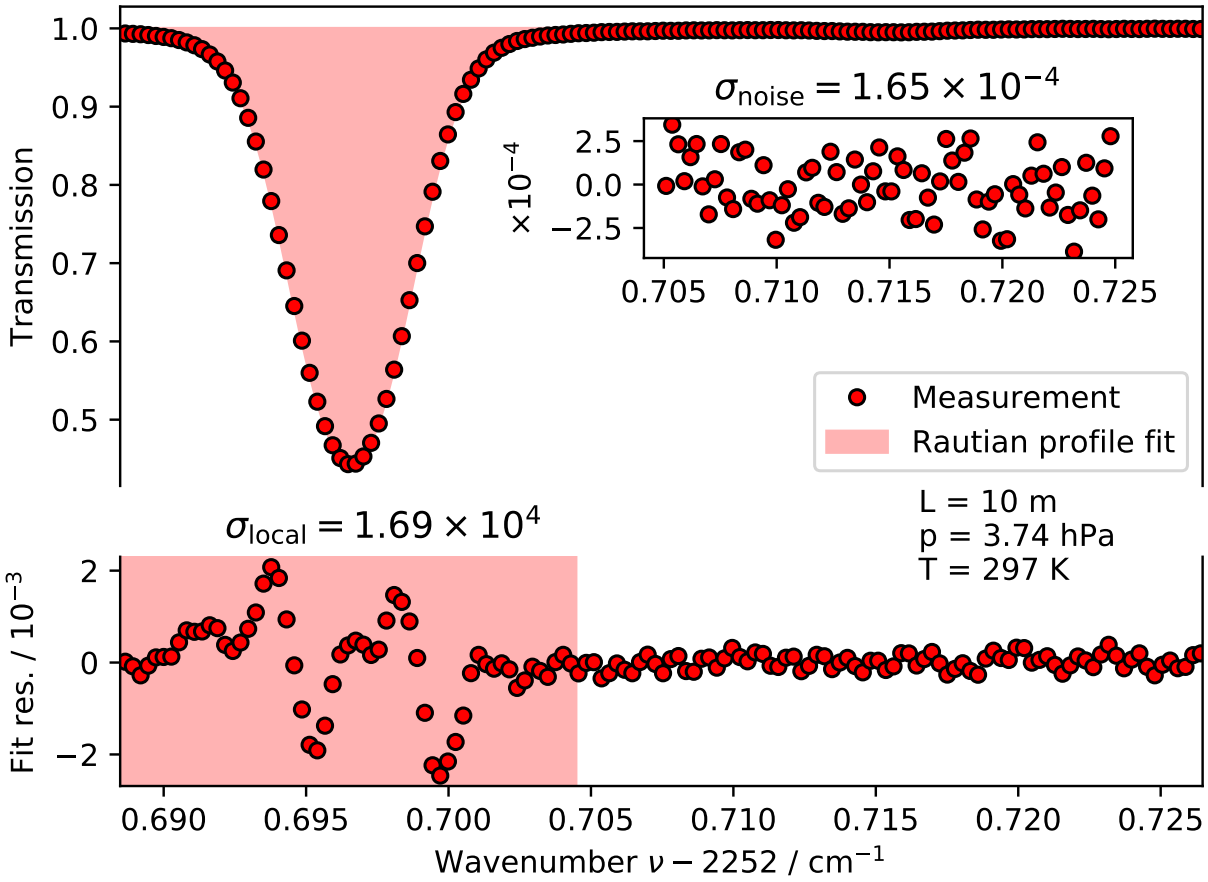

Figure 4: Zoomed part of the measured transmission spectrum of $^{13}C^{16}O^{18}O$ transition around $2252.7\,\mathrm{cm}^{-1}$. The inset shows the noise of the baseline. Lower part depicts line fit residuals.

The use of mid-IR optical fibers in our system is justified by two reasons: first, to avoid absorption in the background air-CO_2 of free space between the laser and the cell, second,

it allow to thermally decouple laser housings and gas cell, which have to be stabilised at different temperatures. This type of fibers are usually used in combustion studies[30,31] for remote delivery of laser light. The fiber optics layout has additional optical elements, hence increased number of surfaces, compared to layouts where a system of mirrors is used for light delivery to the gas cell. It is potentially dangerous with respect to formation of spectral fringes. Furthermore, 1 m InF_3 fibers (refractive index $n = 1.48$) gives interference fringes of $3.3 \times 10^{-3}\,\mathrm{cm}^{-1}$, which is on the same order as characterisic absorption line width of our experiment. Careful optical train alignment and optical fiber light coupling is required to minimise the etalon effects, at times in expense of coupling efficiency. As mentioned above in this section, the spectral noise of our spectrometer is comparable to the systems that have no fibers.

Sample handling and gas inlet system

Figure 5 shows the semi-automatic gas handling and inlet system that has been developed for the preparation of CO_2 samples. This system is coupled to the optical instrument described above. The vacuum system is constructed out of Swagelok electropolished stainless steel tubing (OD=6 mm) and 12 pneumatically operated diaphragm valves (TK-Fujikin) operated by a custom built controller. An in-house developed LabView program is used to operate the valves and monitor the pressure readings of three gauges. An adjustable bellow with a volume between 50 and 300 cm^3 is installed on the reference side of the inlet. It allows to control the expansion volume and balance the pressure of reference and sample gas at a relative level of 10^{-3}. Two heated capacitance manometers (MKS Baratron 627) with 10 Torr and 100 hPa full scale ranges monitor the pressure in the optical cell and the expansion volume, respectively. A dry scroll pump and a turbo-molecular pump are used to evacuate the inlet system and the optical cell. The typical background pressure in the system is about 2×10^{-6} hPa. Evacuation from 4 hPa down to 5×10^{-6} hPa takes up to 200 seconds, and the leak rate is below 1×10^{-6} hPa/h.

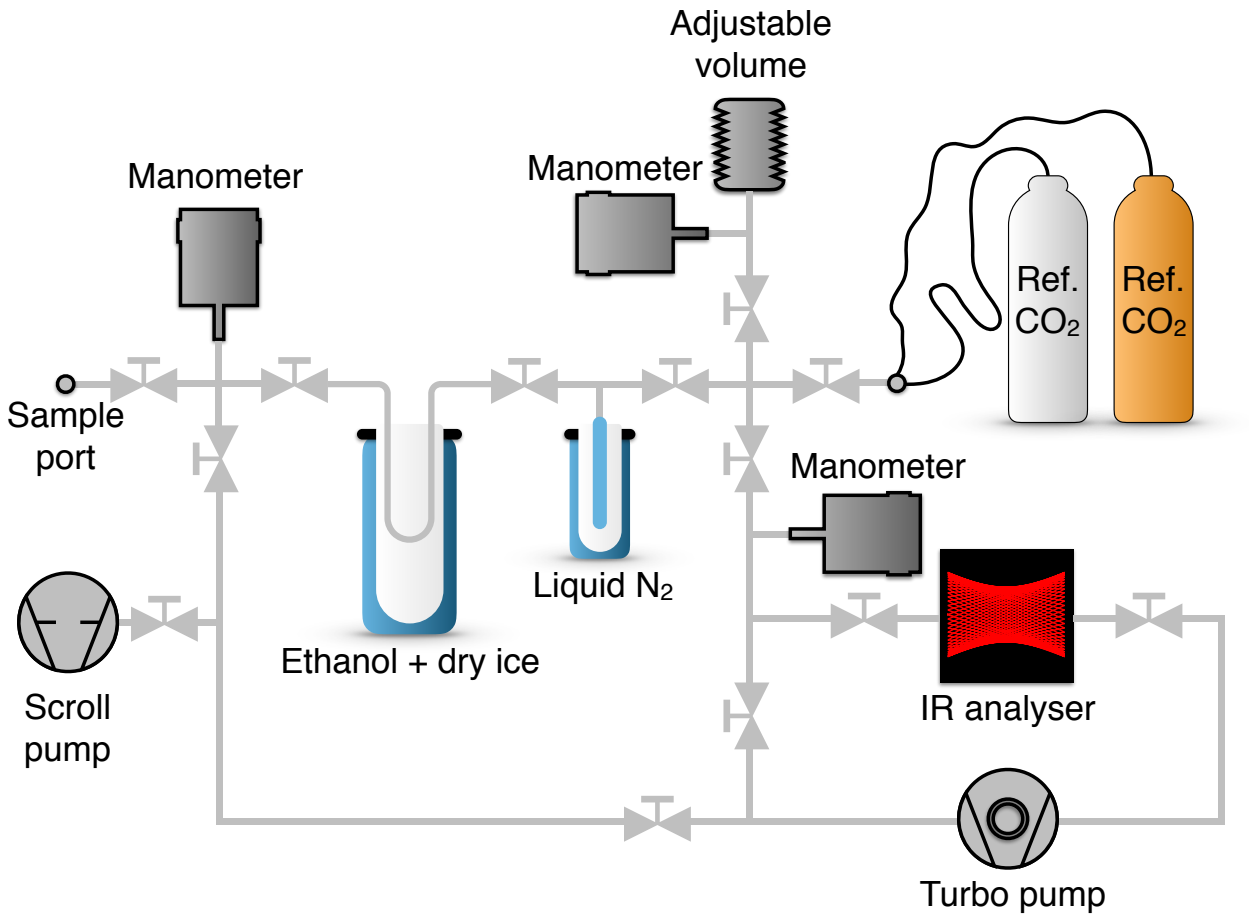

Figure 5: Layout of the vacuum system employed for CO_2 sample handling.

The sample is introduced to the system via a Swagelok VCR connection. At the first stage of sample preparation, potential trace water contamination is removed by a $-70\,°C$ U-shaped trap immersed in an ethanol and dry ice mixture. The second cryogenic trap at $-196\,°C\,(LN_2)$ is made of a quartz tube. The CO_2 sample is stored between measurements and cryogenically separated from non-condensable contaminants during the preparation in this trap. No re-equilibration of the CO_2 isotope signature within 1×10^{-5} has been observed in the system over a time period of 20 h. Two high pressure gas bottles of CO_2 with significantly different isotopic compositions (Air Liquide, N4.8, $\delta^{13}C_{VPDB} = -40.28‰$, $\delta^{18}O_{VPDB-CO_2} = -27.04‰$ and Thermo Scientific, N4.5, $\delta^{13}C_{VPDB} = -9.75‰$, $\delta^{18}O_{VPDB-CO_2} = -17.10‰$) were attached to the system. These gases allowed to perform

regular instrument calibration and served as working reference gases (WRG).

Results and discussion

Instrument stability

A prolonged measurement series (1000 seconds) has been acquired in order to perform an analysis of the instrumental stability. The Allan deviation plot of two absorption ratios measured simultaneously is shown in Figure 6. Spectra are averaged over 1 second and fitted by a Rautian[32] profile with fixed Doppler γ_D and Lorentz γ_L parameters.[26] The optical baseline in the empty cell has been measured for 10 seconds before the injection of 3 hPa of pure CO_2. White noise dominates the system on the time scale of 10 seconds; the ultimately achieved relative precision level is $\sim 2 \times 10^{-5}$. Drifts become important on timescales above 100 seconds. Based on this behaviour of the system, the measurement time has been set to 20 seconds. One cycle of reference and sample gas comparison should be performed on the time scale of 100 seconds.

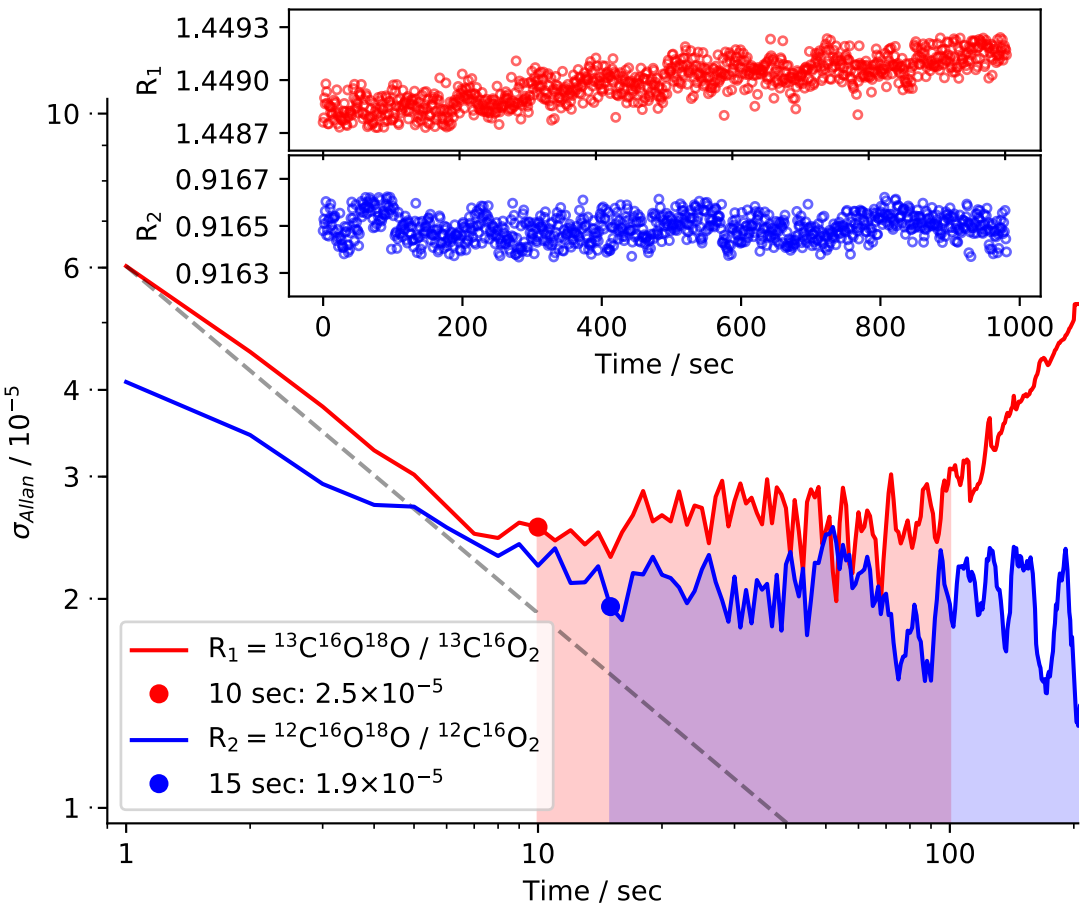

Figure 6: Allan deviation plot and associated time series of two absorption intensity ratios $R_1 = A(^{13}C^{16}O^{18}O)/A(^{13}C^{16}O_2)$, $R_2 = A(^{12}C^{16}O^{18}O)/A(^{12}C^{16}O_2)$ measured simultaneously by two lasers at 1 Hz rate. Shaded areas indicate targeted measurement times.

Reproducibility and analytical strategy

One measurement cycle consists of the following steps: 1) The cell is evacuated down to the background pressure of 4×10^{-6} hPa, and the zero absorption baseline is acquired over 10 seconds. 2) The reference gas is filled into the cell within 5 seconds and spectra are acquired over 20 to 30 seconds with a typical cell pressure of 3 to 4 hPa. 3) The reference gas is evacuated from the cell, which takes between 100 and 150 seconds. 4) The sample gas is released into the gas cell and absorption spectra are recorded. 5) The sample is cryogenically extracted from the vacuum chamber to the quartz freezing finger and stored there for repetitive analysis. The whole procedure takes typically 7 minutes.

To test the repeatability of the established method a white noise measurement series of $n = 19$ consecutive, independent self comparisons of the working gas (wrg) has been performed (Figure 7). The top panel of Figure 7 depicts the measured values of the integrated line absorbances, where $R_1 = (^{13}C^{16}O^{18}O)/(^{13}C^{16}O_2)$, $R_2 = (^{12}C^{16}O^{18}O)/(^{12}C^{16}O_2)$. A pronounced drift is evident in the R_1/R_2 series, possibly due to temperature and pressure fluctuations, and long term optical instabilities of the system. This series has a standard deviation of 0.2×10^{-3}. The pressure $p = 3.74\,\mathrm{hPa}$ has been controlled at the $1 \times 10^{-3}\,\mathrm{hPa}$ level and the temperature around $T = 297\,\mathrm{K}$ was stabilised within 2 mK.

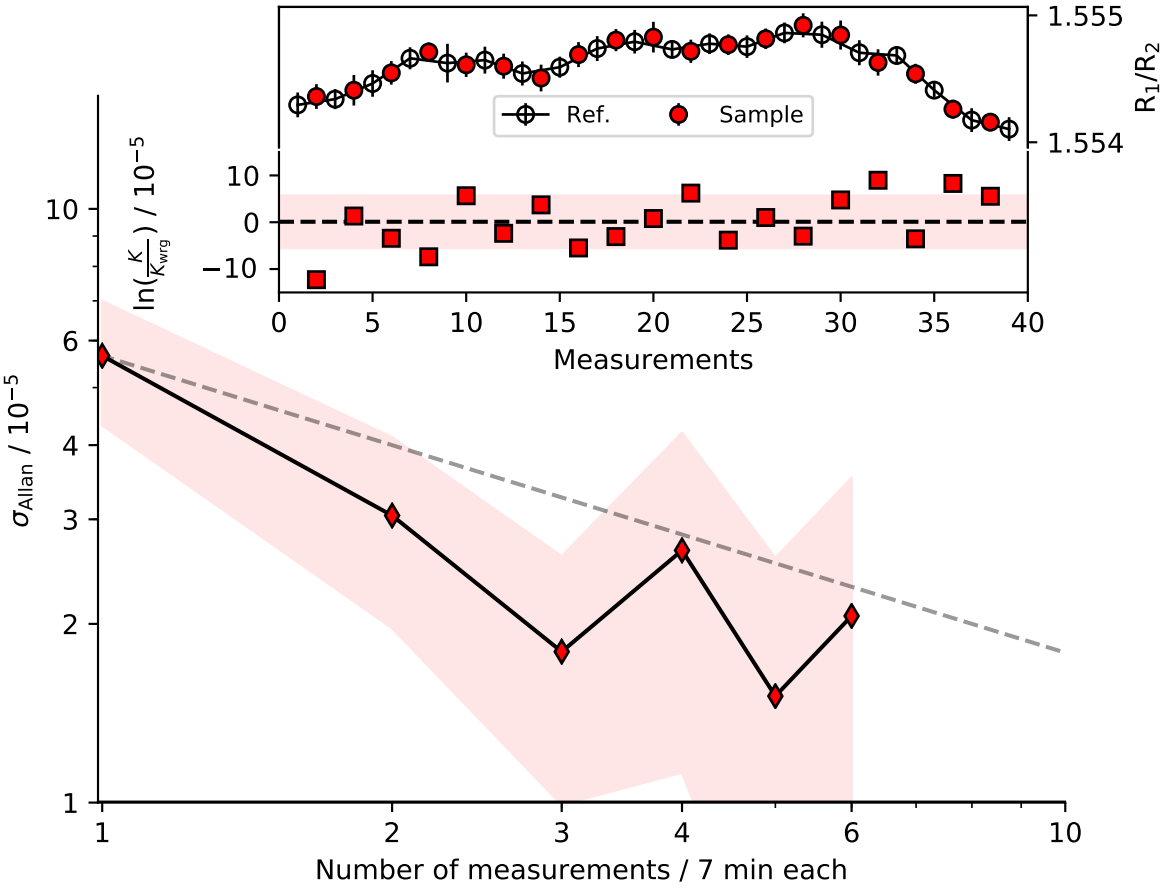

Figure 7: Top panel: a prolonged measurement series of the absorbance ratio (red and black circles) and the logarithmic ratio of two consecutive absorbance ratios (red squares). Lower panel: Allan deviation plot of the logarithmic ratio series (red diamonds). The dashed line presents white noise behaviour.

For $\ln(K/K_{\mathrm{wrg}})$ defined in Eq. 1 and evaluated as a logarithmic ratio of two consecutive

R_1/R_2 values, the standard deviation is $1\sigma = 56 \times 10^{-6}$, and the standard error of the mean 1SEM = 13×10^{-6} (n=19). The mean $\ln(K/K_{\mathrm{wrg}})$ value of the series is 1×10^{-6}.

Using the same experimental setting, two working reference gases with different isotopic compositions have been compared. The first measurement series consisted of $n = 5$ independent analyses, yielding an average equilibrium constant of $\ln(K_{\mathrm{wrg1}}/K_{\mathrm{wrg2}}) = 112 \times 10^{-6}$, with standard deviation of $\sigma_{n-1} = 50 \times 10^{-6}$ and corresponding standard error of the mean SEM = 22×10^{-6}. The second experimental series was conducted 3 months after the first one and consisted of $n = 6$ analyses, with a measured value of 124×10^{-6}, $\sigma_{n-1} = 37 \times 10^{-6}$, 1SEM = 15×10^{-6}. A similar precision has been obtained for the δ values of singly substituted isotopologues, except $^{12}C^{16}O^{17}O$, whose precision is on the level of 150×10^{-6} (1σ).

The Allan deviation presented in Figure 7 indicates that a precision of 1×10^{-5} usually reported for state of the art precision of isotope ratio mass spectrometers[33,34] can be achieved after 36 repetitive analyses. In the present experimental setup, this corresponds to 4 h of instrument operation. This duration is compatible with the typical analysis time of a conventional dual inlet mass spectrometer.[15]

Calibration and correction

For instrument calibration CO_2 gases with known isotope signature corresponding to a certain equilibrium temperature were prepared.

An almost stochastic distribution of isotopologues $K/K^* = 1$ can be realised by heating CO_2 gas to temperatures above 2000 °C. As these conditions are difficult to realise experimentally, gases were equilibrated at $T = 1000$ °C by heating pure dry CO_2 aliquots in sealed ampules. The ampules were made of quartz (Ovisil) tubes with outer diameter of 11 mm and length of 50 mm. The pre-treatment of the glass tubes involved vacuum evacuation down to 3×10^{-5} hPa over at least 12 hours. The tubes were then filled with 0.6 bar pure dry CO_2 and sealed with a natural gas-oxygen torch. Each ampule contained approximately 100 µmol of carbon dioxide. The sealed tubes were subsequently heated in a furnace at 1000 °C over

$4-5$ hours and then quenched in liquid nitrogen. The gas was released from the ampule by mechanical cracking under low vacuum conditions (2×10^{-3} hPa) and cryogenically collected in the system presented in Figure 5. The spectroscopic analysis was performed within less than one hour after quenching the ampule.

Whilst close to random distribution can be reached within a reasonable time of several hours[35], isotope distributions that reflect intermediate temperatures are only hardly achieved when pure dry gas undergoes continuous heating or cooling. A convenient way to modify the isotopologue distribution is to enhance oxygen isotope exchange with water[17,35,36]. These samples were thus prepared by adding 0.5 ml (25 mmol) of water with known oxygen isotope signature to 100 µmol of pure CO_2. The mixture was sealed in 6 mm outer diameter Pyrex tubes and stored at the desired equilibration temperature for several hours to several days in an oven or over a number of weeks in a cold bath. After cryogenic separation from potential water traces, the pure gas from the headspace of the tube is released and cryogenicallly collected in the gas handling system.

Figure 8 shows the result of the experiment aimed at studying the influence of bulk isotopic composition on the experimentally measured raw logarithmic equilibrium constants ratio $\ln(K/K_{\mathrm{wrg}})$. A shallow slope of about -3×10^{-4} has been observed on a $\ln(K/K_{\mathrm{wrg}}) - \delta^{18}\mathrm{O}$ diagram (blue axis in Figure 8). This slope was obtained by measurements of the samples equilibrated at T=+1 °C with waters of different $\delta^{18}\mathrm{O}$ and identical $\delta^{13}\mathrm{C}$. For natural abundances of $^{18}\mathrm{O}$, the maximum $\delta^{18}\mathrm{O}_{\mathrm{wrg}}$ can be estimated on the level of $50‰=5 \times 10^{-2}$ which might lead to insignificant correction of 1.5×10^{-5} for $\ln(K/K_{\mathrm{wrg}})$ measurements. A steeper slope has been observed for $\ln(K/K_{\mathrm{wrg}}) - \delta^{13}\mathrm{C}$ (red axis in Figure 8). A series of experiments with heated gases and room temperature bottle gases has been conducted to determine the correction coefficient $\ln K/\delta^{13}\mathrm{C} = -3.85 \times 10^{-3}$. A likely explanation of this dependence is that the spectral window centered around 2252.7 cm^{-1} is located between two strong $^{13}\mathrm{C}^{16}\mathrm{O}_2$ lines from the ν_3 fundamental band. The background absorption is influenced by the tails of these strong lines in the vicinity of the lines used for the detection

of the $^{13}C^{16}O^{18}O/^{13}C^{16}O_2$ ratio. Therefore, the variation of carbon isotopic composition, that has a first order effect on the abundance of $^{13}C^{16}O_2$ isotopologue, causes a variation of the background absorption level. This effect is likely not fully taken into account in the fitting model, and is currently parametrised through the linear correction with constant coefficient.

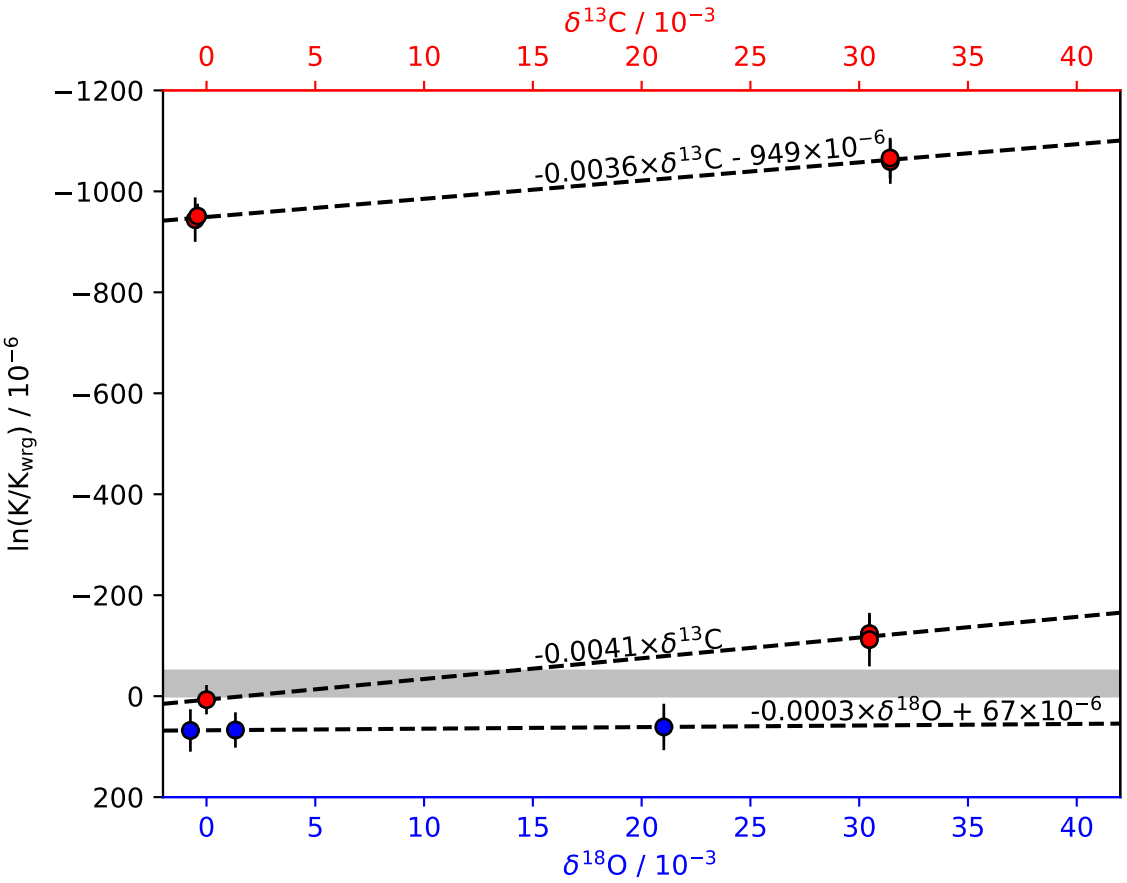

Figure 8: Dependence of the logarithmic equilibrium constant ratio $\ln(K/K_{\mathrm{wrg}})$ on the difference in isotopic composition (δ^{13}C and δ^{18}O) between sample and reference gas. Grey shaded area represents typical reproducibility on the level of 5×10^{-5}.

Similar influence of singly substituted isotopologue concentration on doubly-substituted isotopologue measurements has been observed earlier for $^{13}CH_3D$ measurements.[37] Accuracy of stable isotope analysis in air-CO_2 is also limited by mole fraction dependence.[38,39] Thus, a proper choice of the reference gas, whose isotopic composition is close to the expected isotopic composition of the sample, can minimise the uncertainty associated with this effect.

As indicated by the grey shaded area in the Figure 8, the mismatch between sample and reference below 15‰ in δ^{13}C levels off the effect on the level below the typical measurements reproducibility.

Comparison with isotope ratio mass spectrometry

The instrument performance has been compared to IRMS using selected samples. Table 2 and Figure 9A, B show the δ^{13}C and δ^{18}O values of the the working reference gases and carbonate-CO_2 measured with isotope ratio mass spectrometry (IRMS) and direct laser absorption spectroscopy (DLAS). WRG1 is pure CO_2 supplied by Thermo Scientific, the isotopic composition provided by the manufacturer is $\delta^{13}C_{VPDB} = -9.86(15)‰(1\sigma)$, $\delta^{18}O_{VPDB\text{-}CO_2} = -17.25(15)‰(1\sigma)$. This gas has been used as a working reference gas for all DLAS measurements presented in this chapter. The second working reference gas (WRG2) is a high purity (N4.8) CO_2 from Air Liquide. The difference between the isotopic δ values of WRG2 identified with IRMS and DLAS might indicate the scale contraction of spectroscopic measurements, the best estimates are $\delta^{18}O = 0.9935 \times \delta^{18}O_{DLAS}$ and $\delta^{13}C = 1.0019 \times \delta^{13}C_{DLAS}$. ISO-GAS-1 and ISO-GAS-2 are two working reference gases which are routinely used in the Institute of Environmental Physics, University of Heidelberg. The observed differences in δ^{13}C and δ^{18}O of at maximum 0.3‰ for these gases can be explained by the fractionation effects during the sample handling and transportation. ISO-CARB-1 and ISO-CARB-2 are two carbon dioxide aliquots liberated from 10 mg of carbonates by acid digestion at 90 °C. Details of carbonate reaction and IRMS measurements are described elsewhere.[40] Isotope delta values are consistent between both methods over the full evaluated isotopic range with few deviations not exceeding 0.3‰.

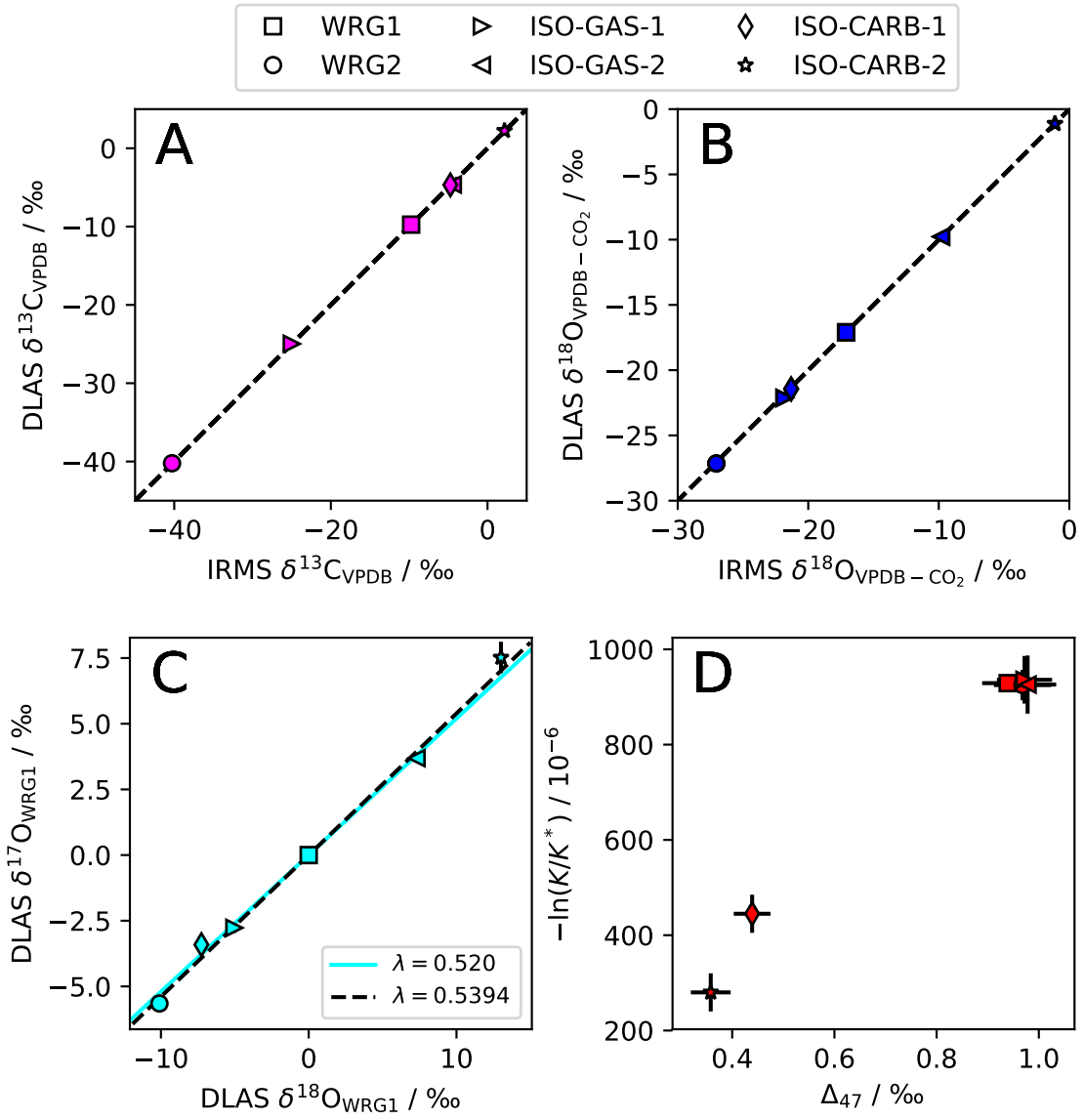

Figure 9: Results of $\delta^{13}C_{VPDB}$ (A) and $\delta^{18}O_{VPDB-CO2}$ (B) measurements performed with DLAS versus respective IRMS measurements. (C) $\delta^{17}O$ versus $\delta^{18}O$ measured with DLAS. (D) Δ_{47} and $-\ln(K/K*)$ values of six gas samples (Table 2).

One of the advantages of the optical method is the possibility to directly measure the line of the $^{12}C^{16}O^{17}O$ isotopologue and, therefore, $\delta^{17}O$, this was demonstrated earlier by Stoltmann et al.[41] and Sakai et al.[42]. Mass spectrometric analysis of CO_2 isotopologues with substituted ^{17}O are only possible if the isobaric interference with more abundant ^{13}C substituted isotopologue of CO_2 can be resolved or if a different technique is used (e.g.,

reduction and fluorination[43]). Although the presented spectroscopic instrument was not optimised to perform a $\delta^{17}O$ analysis, our pilot study has been conducted using the weak $^{12}C^{16}O^{17}O$ transition in the vicinity of the main isotopologue transition at 2310.00 cm^{-1} (see Table 1 and Figure 3). Figure 9C and Table 2 show $\delta^{17}O$ with respect to the $^{17}O/^{16}O$ ratio of the working reference gas WRG1. The $\delta^{17}O - \delta^{18}O$ slope obtained from the linear regression of the measured values is $\lambda = 0.5394 \pm 0.0097(1\sigma)$, with corresponding 95% confidence interval (3 DOF) of 0.506 - 0.568. Our estimations are in agreement with the expected value $\lambda = 0.52$[34,44]. Compared to $^{12}C^{16}O^{18}O$, the accurate fitting of a weak line of $^{12}C^{16}O^{17}O$ isotopologue is more challenging due to the decreased signal-to-noise ratio and more pronounced contribution of the tails of neighboring lines. In order to optimise the instrument for $\Delta^{17}O$ or $\delta^{17}O$ measurements, a spectral window with an isolated $^{12}C^{16}O^{17}O$ line, which fulfils the criteria mentioned earlier, would need to be selected and implemented. Nevertheless, the current configuration of the instrument can already be used for direct $\delta^{17}O$ measurements with a typical precision of $\pm 0.1‰$.

The clumped isotope Δ_{47} values for the samples presented in Table 2 have been compared with the logarithmic equilibrium constants $\ln(K/K^*)$ (Figure 9D). The apparent equilibrium temperatures have been reconstructed using the theoretical consideration derived by Wang et al.[1]. The equilibrium constant of the working reference gas has been identified in a separate experiment, where working reference gas from a cylinder has been compared with its aliquote equilibrated at 1000 °C. The value of the logarithmic equilibrium constant for heated gas was assigned to $\ln(K) = -26 \times 10^{-6}$. Although the stochastic distribution of isotopologues is not realised at this temperature, the uncertainty of the assigned value is smaller than the analytical precision of the instrument.[16] A correction for $\delta^{13}C$ difference between sample and reference (Figure 8) has been applied for all samples. Both methods (DLAS and IRMS) show that the equilibrium temperatures of the reference gases are in the room temperature range and agree with each other within 1σ uncertainty. The CO_2 samples liberated from carbonates have apparent equilibrium temperatures of 178 °C and

250 °C, respectively. Typical uncertainties of the estimated temperatures are ±8 °C at 25 °C and ±25 °C at 250 °C.

Table 2: Isotopic composition $\delta^{13}C_{VPDB}$ and $\delta^{18}O_{VPDB\text{-}CO_2}$ measured with direct laser absorption spectroscopy (DLAS) and isotope ratio mass spectrometry (IRMS), logarithmic equilibrium constant ratio $\ln(K/K^*)$ and clumped isotope Δ_{47} of pure CO_2 gases from high pressure cylinders: WRG1, WRG2, ISO-GAS-1, ISO-GAS-2; and pure CO_2 liberated from carbonates: ISO-CARB-1, ISO-CARB-2. Relative variation $\delta^{17}O_{WRG1}$ is measured with respect to working reference gas (WRG1). Apparent equilibrium temperatures are calculated using theoretical dependencies presented in Wang et al.[1] Uncertainties for DLAS and IRMS are given as standard deviation (1σ) of 4 and 8 measurements, respectively, indicated in parentheses. All δ and Δ_{47} values are given in ‰, $\ln(K/K^*)$ is multiplied by a factor of -1×10^6, temperature is reported in °C.

Sample	$\delta^{13}C_{VPDB}$		$\delta^{18}O_{VPDB\text{-}CO_2}$		$\delta^{17}O_{WRG1}$	Δ_{47}	$T_{\Delta_{47}}$	$\ln(K$
	IRMS	DLAS	IRMS	DLAS				
WRG1	−9.75(1)	−9.75	−17.10(1)	−17.10	0.00	0.939(50)	20^{+9}_{-8}	929
WRG2	−40.28(1)	−40.22(3)	−27.04(1)	−27.15(4)	−5.65(9)	0.968(56)	15^{+10}_{-9}	925
ISO-GAS-1	−24.99(5)	−24.97(15)	−21.82(11)	−22.13(7)	−2.77(19)	0.972(54)	14(9)	936
ISO-GAS-2	−4.43(1)	−4.63(5)	−9.82(1)	−9.77(4)	3.69(15)	0.978(56)	13^{+10}_{-9}	926
ISO-CARB-1	−4.74(4)	−4.68(4)	−21.31(10)	−21.44(10)	−3.41(36)	0.430(36)	175^{+19}_{-17}	445
ISO-CARB-2	2.17(11)	2.24(1)	−1.10(14)	−1.12(11)	7.52(60)	0.358(39)	216^{+26}_{-23}	280

The demonstrated performance of the optical carbon dioxide isotopologue thermometer and its compatibility with the established mass spectrometric technique allows it to be applied to a number of environmental applications, where clumped isotope IRMS methods are already used, and may in future open up new and promising application fields.[16]

Conclusion

We have developed a new laser spectrometer for direct and accurate detection of the five most abundant isotopologues of CO_2. This instrument provides a unique proxy-thermometer, the logarithmic equilibrium constant ration $\ln(K/K^*)$. The mid-IR spectrometer operates in the ν_3 band of CO_2 and is equiped with the gas inlet system designed for repetitive analysis

of pure gas phase carbon dioxide samples. Achieved precision of a single isotopologue ratio measurement is on the level of 2×10^{-5} after 15 seconds of integration, the reproducibility of the equilibrium constant ratio is better than $5 \times 10^{-5}(1\sigma)$. A calibration strategy based on measurements of CO_2 with different isotopic compositions from equilibration at different temperatures has been implemented. The instrument is also capable of $\delta^{13}C$, $\delta^{18}O$ and $\delta^{17}O$ measurements with precisions of 0.05‰, 0.05‰ and 0.15‰, respectively. The typical measurement time are comparable to modern commercially available isotope ratio mass spectrometers for clumped isotope analysis. The required sample size is on the level of 100 µmol. The advantages of the optical realisation, i.e. lower cost, smaller size, ease of applicability to different molecular systems ($^{15}N^{14}N^{18}O$, $^{13}C^{16}O^{17}O$, $^{12}C^{18}O_2$, etc) and the capability of analysis in multi-component systems, e.g. $^{13}C^{16}O^{18}O$ in air, open up new perspectives for application in environmental sciences and fundamental research.

Aknowledgements

I.P. and T.K. acknowledge funding from the Heidelberg Graduate School of Fundamental Physics (HGSFP). C.J. acknowledges Norbert Frank for invitation to a visiting professorship at IUP Heidelberg during a short period of this work. We acknowledge the technical help of the 'physics of environmental archives' team to maintain the IRMS instrument that was funded through the grant DFG-INST 35/1270-1 The authors acknowledge Hadj Elandaloussi, Pascal Jeseck, and Christian Rouillé for technical support, Patrick Marie-Jeanne for optical cell construction, and the central mechanical workshop of Heidelberg University for help in the vacuum chamber development.

References

(1) Wang, Z.; Schauble, E. A.; Eiler, J. M. *Geochimica et Cosmochimica Acta* **2004**, *68*, 4779–4797.

(2) Ghosh, P.; Adkins, J.; Affek, H.; Balta, B.; Guo, W.; Schauble, E. a.; Schrag, D.; Eiler, J. M. *Geochimica et Cosmochimica Acta* **2006**, *70*, 1439–1456.

(3) Schauble, E. A.; Ghosh, P.; Eiler, J. M. *Geochimica et Cosmochimica Acta* **2006**, *70*, 2510–2529.

(4) Yeung, L. Y. *Geochimica et Cosmochimica Acta* **2016**, *172*, 22–38.

(5) Röckmann, T. et al. *Scientific Reports* **2016**, *6*, 31947.

(6) Eiler, J. M. *Earth and Planetary Science Letters* **2007**, *262*, 309–327.

(7) Eiler, J. M.; Clog, M.; Magyar, P.; Piasecki, A.; Sessions, A.; Stolper, D.; Deerberg, M.; Schlueter, H. J.; Schwieters, J. *International Journal of Mass Spectrometry* **2013**, *335*, 45–56.

(8) Eagle, R. A.; Enriquez, M.; Grellet-Tinner, G.; Pérez-Huerta, A.; Hu, D.; Tütken, T.; Montanari, S.; Loyd, S. J.; Ramirez, P.; Tripati, A. K.; Kohn, M. J.; Cerling, T. E.; Chiappe, L. M.; Eiler, J. M. *Nature Communications* **2015**, *6*, 8296.

(9) Came, R. E.; Brand, U.; Affek, H. P. *Chemical Geology* **2014**, *377*, 20–30.

(10) Kluge, T.; Affek, H. P. *Quaternary Science Reviews* **2012**, *49*, 82–94.

(11) Affek, H. P.; Eiler, J. M. *Geochimica et Cosmochimica Acta* **2006**, *70*, 1–12.

(12) Yeung, L. Y.; Affek, H. P.; Hoag, K. J.; Guo, W.; Wiegel, A. A.; Atlas, E. L.; Schauffler, S. M.; Okumura, M.; Boering, K. A.; Eiler, J. M. *Proceedings of the National Academy of Sciences of the United States of America* **2009**, *106*, 11496–501.

(13) Wang, D. T.; Welander, P. V.; Ono, S. *Geochimica et Cosmochimica Acta* **2016**,

(14) Yeung, L. Y.; Young, E. D.; Schauble, E. A. *Journal of Geophysical Research: Atmospheres* **2012**, *117*, n/a–n/a.

(15) Huntington, K. W.; Eiler, J. M.; Affek, H. P.; Guo, W.; Bonifacie, M.; Yeung, L. Y.; Thiagarajan, N.; Passey, B.; Tripati, A.; Daëron, M.; Came, R. *Journal of Mass Spectrometry* **2009**, *44*, 1318–1329.

(16) Prokhorov, I.; Kluge, T.; Janssen, C. *Scientific Reports* **2019**, *9*, 4765.

(17) Dennis, K. J.; Affek, H. P.; Passey, B. H.; Schrag, D. P.; Eiler, J. M. *Geochimica et Cosmochimica Acta* **2011**, *75*, 7117–7131.

(18) Kerstel, E.; Gianfrani, L. *Applied Physics B* **2008**, *92*, 439–449.

(19) Gordon, I. et al. *J. Spectrosc. Rad. Trans.* **2017**, *203*, 3 – 69, HITRAN2016 Special Issue.

(20) Tuzson, B.; Zeeman, M.; Zahniser, M.; Emmenegger, L. *Infrared Physics & Technology* **2008**, *51*, 198–206.

(21) Nelson, D. D.; Mcmanus, B. J.; Zahniser, M. S. *Applied Physics B* **2008**, *90*, 301–309.

(22) Croizé, L.; Mondelain, D.; Camy-Peyret, C.; Delmotte, M.; Schmidt, M. *Review of Scientific Instruments* **2008**, *79*, 043101.

(23) Uehara, K.; Yamamoto, K.; Kikugawa, T.; Yoshida, N. *Sensors and Actuators B: Chemical* **2001**, *74*, 173 – 178, Proceedings of the 5th European Conference on Optical Chemical Sensors and Biosensors.

(24) McManus, J.; Zahniser, M. S.; Nelson, D. D.; Williams, L. R.; Kolb, C. E. *Spectrochimica Acta Part A: Molecular and Biomolecular Spectroscopy* **2002**, *58*, 2465 – 2479.

(25) Minissale, M.; Zanon-Willette, T.; Prokhorov, I.; Elandaloussi, H.; Janssen, C. *IEEE Transactions on Ultrasonics, Ferroelectrics, and Frequency Control* **2018**, *65*, 1487–1491.

(26) Tennyson, J. et al. *Pure and Applied Chemistry* **2014**, *86*, 1931–1943.

(27) Ngo, N.; Lisak, D.; Tran, H.; Hartmann, J.-M. *Journal of Quantitative Spectroscopy and Radiative Transfer* **2013**, *129*, 89 – 100.

(28) McManus, J. B.; Zahniser, M. S.; Nelson, D. D.; Shorter, J. H.; Herndon, S. C.; Wood, E. C.; Wehr, R. *Optical Engineering* **2010**, *49*, 111124.

(29) Graf, M.; Emmenegger, L.; Tuzson, B. *Opt. Lett.* **2018**, *43*, 2434–2437.

(30) Spearrin, R. M.; Goldenstein, C. S.; Jeffries, J. B.; Hanson, R. K. *Measurement Science and Technology* **2013**, *24*, 055107.

(31) Spearrin, R. M.; Ren, W.; Jeffries, J. B.; Hanson, R. K. *Applied Physics B: Lasers and Optics* **2014**, *116*, 855–865.

(32) Rautian, S. G.; Sobel'man, I. I. *Physics-Uspekhi* **1967**, *9*, 701–716.

(33) Dennis, K. J.; Schrag, D. P. *Geochimica et Cosmochimica Acta* **2010**, *74*, 4110–4122.

(34) Daëron, M.; Blamart, D.; Peral, M.; Affek, H. *Chemical Geology* **2016**, *442*, 83–96.

(35) Affek, H. P. *American Journal of Science* **2013**, *313*, 309–325.

(36) Clog, M.; Stolper, D.; Eiler, J. M. *Chemical Geology* **2015**, *395*, 1–10.

(37) Ono, S.; Wang, D. T.; Gruen, D. S.; Lollar, B. S.; Zahniser, M. S.; Mcmanus, B. J.; Nelson, D. D. *Analytical Chemistry* **2014**, *86*, 6487–6494.

(38) Flores, E.; Viallon, J.; Moussay, P.; Griffith, D. W. T.; Wielgosz, R. I. *Analytical Chemistry* **2017**, *89*, 3648–3655.

(39) Griffith, D. W. T. *Atmospheric Measurement Techniques* **2018**, *11*, 6189–6201.

(40) Kluge, T.; John, C. M.; Jourdan, A.-L.; Davis, S.; Crawshaw, J. *Geochimica et Cosmochimica Acta* **2015**, *157*, 213 – 227.

(41) Stoltmann, T.; Casado, M.; Daëron, M.; Landais, A.; Kassi, S. *Analytical Chemistry* **2017**, *89*, 10129–10132.

(42) Sakai, S.; Matsuda, S.; Hikida, T.; Shimono, A.; McManus, J. B.; Zahniser, M.; Nelson, D.; Dettman, D. L.; Yang, D.; Ohkouchi, N. *Analytical Chemistry* **2017**, *89*, 11846–11852.

(43) Passey, B. H.; Hu, H.; Ji, H.; Montanari, S.; Li, S.; Henkes, G. A.; Levin, N. E. *Geochimica et Cosmochimica Acta* **2014**, *141*, 1 – 25.

(44) Bao, H.; Cao, X.; Hayles, J. A. *Annual Review of Earth and Planetary Sciences* **2016**, *44*, 463–492.

Graphical TOC Entry